Statistical Characterization of GITM Thermospheric Horizontal Winds in Comparison to GOCE Estimations

Daniel A. Brandt[1], **Aaron J. Ridley**[2]

[1]Michigan Tech Research Institute
[2]Department of Climate and Space Science and Engineering, University of Michigan - Ann Arbor

Key Points:

- Cross-track horizontal winds from GOCE are compared to GITM for Jan-Oct 2013.
- GITM captured the overall distribution of horizontal winds, but with lower means than GOCE.
- GITM overpredicts horizontal wind in the equatorial ionization anomaly regions.

Corresponding author: Daniel A. Brandt, `branddan@umich.edu`

Abstract

Characterization of the thermospheric horizontal wind is an important challenge in atmospheric modeling, due to its vital role in the transport of densities and energy, associations with the diurnal tide, and interplay with vertical winds that drive changes in the thermosphere neutral composition. The mechanisms and drivers that underlie the physics of thermospheric horizontal winds remain under investigation and, to date, no comprehensive statistical study between thermospheric winds generated by a physics-based atmospheric model and those retrieved from satellite measurements has been performed. Comparisons between cross-track horizontal winds from a 10-month run of GITM and those derived from the Gravity field and steady-state Ocean Circulation Explorer (GOCE) satellite showed that GITM's modeled horizontal winds best in the polar zone and overestimated them at midlatitudes in the equatorial ionization anomaly region. GITM's wind response to AE was best at polar noon and worst in the midnight auroral zone, its ability to capture seasonality was best in the northern high latitudes and worst in the southern high latitudes, and GITM displayed less wind variability as a function of F10.7 than GOCE, matching it best for F10.7$>\sim$ 150. Discrepancies in GITM's performance may be explained by inaccurate modeling of ion drift, ion drag, and electron densities.

Plain Language Summary

Modeling the behavior of the horizontal wind in the thermosphere is an important challenge, since the horizontal wind plays a major role in the dynamics of the thermosphere. Horizontal winds are important because they change the neutral composition of the atmosphere and redistribute energy from the high latitudes towards the equator. While there exist several physics-based models of the atmosphere capable of modeling horizontal winds, there has not yet been a detailed statistical study comparing model results to horizontal wind data from satellites. Data collected by the Gravity field and steady-state Ocean Circulation Explorer (GOCE) satellite show that behavior of the horizontal wind is related to geomagnetic activity, magnetic latitude, and magnetic local time. We evaluated the capability of the Global Ionosphere-Thermosphere Model (GITM) to capture that behavior through a statistical analysis of the horizontal wind. We show that GITM performs best at higher levels of activity in the auroral region and worse in the equatorial anomaly region.

1 Introduction

Horizontal winds in the thermosphere transport gradients in density, composition, and temperature, and play an important role in the global thermospheric circulation. The importance of horizontal winds can be seen in that their divergence and convergence can drive vertical flows, density and composition changes, and changes in temperature (Prölss (1980), (Smith, 1998), and Burns et al. (1991)). Their interactions with ions like O_2^+, NO^+ and O^+ can drive frictional temperature changes as well as field-aligned flows (Guo et al., 2018), and they can push ions across field lines, driving electrodynamical changes in the F-region ionosphere (Billett et al., 2020). While it is clear that winds are critical in describing the thermosphere and ionosphere, there are not many measurements of them, and model validation studies of the winds are few and far between. Since the neutral wind is an important means by which the atmosphere reacts to momentum and heat transfer (Johnson et al., 1995), it plays a vital role in the composition of the thermosphere, especially at the low and middle latitudes (Burns et al., 1989). Convergence and divergence of horizontal winds is also an important mechanism that can produce vertical winds (Rishbeth & Müller-Wodarg, 1999). Therefore, improving understanding of the horizontal winds will lead to an improved understanding of how winds behave in the thermosphere and how thermospheric circulation is impacted by various environmental conditions.

There are a variety of methods for measuring horizontal winds in the thermosphere. Many, such as specular meteor radars and Doppler lidars, are exclusively used on the ground, while others, such as Fabry-Perot interferometers (FPIs), have been used on both the ground and onboard satellites. While each of these methods have their own particular benefits, wind measurements derived from highly-accurate accelerometer measurements onboard low Earth orbit (LEO) satellites present a unique opportunity to study thermospheric winds in depth by virtue of being within the medium of interest itself.

Specular meteor radars detect plasma trails from incoming meteors when their paths lie perpendicular to the radar beam (Ceplecha et al., 1998). Measuring the average Doppler shift allows an observer to infer neutral wind speeds along the radar's line of sight, providing an inexpensive means of generating a dataset of horizontal winds for model development. Recent developments in meteor radar techniques have allowed large radars to be used by following reflections from plasma irregularities that develop from many meteor trails instead of following a single trail with a small radar, and have yielded observations showing wind speeds over 100 m/s between 93 and 110 km using a large VHF radar (Oppenheim et al. (2000) and Oppenheim et al. (2009)). Improvements in calibration and detection techniques have also granted the capability of deriving useful information from nonspecular meteor trails ((Zhao et al., 2011)) and observations from multilink configurations where the radar receivers are not located at the same location as the transmitters ((Chau & Clahsen, 2019)). While this technique can produce high-resolution observations of horizontal winds, it is limited to the upper mesosphere and lower thermosphere and requires as a large VHF radar with interferometric capability.

Horizontal wind measurements are also frequently obtained from Fabry-Perot Interferometer (FPI) observations (Martinis et al. (2001), Oyama et al. (2010), Conde and Smith (1998), and Meriwether et al. (2011)). The speed and direction of the horizontal winds can be obtained by observing the same thermospheric volume at orthogonal look directions from two sites. It is customary to assume a vertical zero-wind reference measurement (J. J. Makela et al. (2013), and Biondi (1984)), or use a stable calibration source, such as a frequency-stabilized HeNe laser (J. Makela et al., 2012). FPIs have been used to show the relationship between horizontal convergence/divergence and changes in the vertical flow (Biondi & Sipler, 1985). Under geomagnetically quiet conditions in the midlatitudes, FPI measurements routinely show wind speeds up to 50 m s^{-1} in the zonal direction and up to 100 m s^{-1} in the meridional direction (Jiang et al., 2018). FPI measurements have additionally shown increased zonal flow and stronger southward meridional flow as a function of increasing altitude, as well as greater absolute wind speeds during the winter (Yuan et al., 2013). They have also been used to study the impact of gravity waves and atmospheric airglow on wind velocity observations in comparison to those obtained with radar techniques (Fujii et al., 2004).

Doppler lidars have been used to study wind and temperature in the mesopause region by detecting the Doppler shift of atomic spectral lines of mesospheric metals such as Na (Bowman et al. (1969), fang Du et al. (2017) and Philbrick et al. (2021)). This technique has seen most applicability using broadband lidars to observe the mesopause region and below, but notable observations of the existence of detectable metals within the lower thermosphere (Gardner et al. (1999), Chu et al. (2011), and Gao et al. (2015)) and the usage of a narrow-band Lidar has enabled observation of winds up to 140 km using this method. Measurements have been shown to be consistent with past rocket measurements (A. Z. Liu et al., 2016).

Satellites in low Earth orbit (LEO) present another source for thermospheric horizontal wind measurements. FPIs have been used aboard satellites such as Dynamics Explorer 2 (DE-2), where they were primarily used to measure the meridional component of the upper thermospheric neutral wind (Killeen et al., 1992). An FPI was also flown aboard the Upper Atmosphere Research Satellite (UARS), where it observed an amplitude of the diurnal tide in the meridional wind larger than that observed by ground-based meteor radars by more than a factor of 2 (Khattatov et al., 1997). The Thermosphere-Ionosphere-Mesosphere Energetics and Dynamics (TIMED) satellite also carries onboard a limb-scanning FPI known as the TIMED Doppler Interferometer (TIDI), which has been used to study migrating diurnal and semidiurnal tides and consistently reproduces ground-based radar observations of the wind (Killeen et al., 2006). The Gravity field and steady-state Ocean Circulation Explorer (GOCE) is another source of horizontal wind data (Floberghagen et al., 2011). The satellite was launched on 17 March 2009, used an ion thruster to sustain its orbit at $\sim$250 km at 96.7° inclination, and reentered the Earth's atmosphere on 11 November 2013 (Strugarek et al., 2019). GOCE's orbit was near sun-synchronous and had a dusk ascending node, and a dawn descending node. GOCE's main payload was the Electrostatic Gravity Gradiometer (EGG), a set of six 3-axis accelerometers mounted in a diamond configuration. The accelerometers of the EGG were 100 times more sensitive than any others previously flown, such as the SuperSTAR accelerometer onboard the GRACE spacecraft (Touboul, 2003). GOCE accelerometer data have been used to investigate the wave coupling between the lower and middle thermosphere (Gasperini et al., 2015), probe the mechanisms driving an eastward wind jet in the evening sector and westward wind jet in the morning sector as well characterizing seasonal variation of the wind (H. Liu et al., 2016), and improve handling of the energy accommodation coefficient to reduce discrepancies when compared to ground-based measurements (Visser et al., 2019a).

Several atmospheric models have been developed and used to simulate the horizontal wind in the thermosphere. The most prominent of these is the Horizontal Wind Model (HWM), which represents the most comprehensive empirical model and describes the atmosphere's vector wind fields from the surface to the exobase as a function of latitude, longitude, altitude, day of year, and time of day. It additionally provides a time-dependent, observationally based, global empirical specification of the upper atmospheric tides and general circulation patterns (Drob et al., 2015). The first version of HWM (HWM87) was generated from thermospheric wind data obtained from the Atmosphere Explorer E and DE-2 satellites, and was limited to above 220 km (Hedin et al., 1988). A subsequent version (HWM90) saw the incorporation of ground-based incoherent scatter radar and FPI data and extension down to 100 km (Hedin et al., 1991), and was succeeded by HWM07, which covers altitudes from the surface to the exosphere and includes representations of zonal means circulation, stationary waves and migrating tides (Drob et al., 2008). Due to the limitations of HWM in modeling storm-time wind activity, a global empirical disturbance wind model (DWM07) was developed that represents averaged geospace-storm-induced perturbations of the upper thermospheric neutral winds, based on data from the Upper Atmospheric Research Satellite, the Dynamics Explorer 2 satellite, and seven ground-based FPIs. The Magnetic mEridional NeuTrAl Thermospheric (MENTAT) model is a recently-developed thermospheric wind model, developed from a global database of ionosonde h_mF_2 observations spanning the years 1961 to 1990, that captures solar cycle wind variation other empirical models fail to reproduce (Dandenault, 2018). The High-latitude Thermospheric Wind Model (HL-TiWM) is another recently-developed empirical model that specifies horizontal neutral winds in the F region at high-latitudes as a function of day of year, latitude, longitude, local time, and geomagnetic activity. It was developed from a several decades of F region FPI measurements and is able to capture the semiannual oscillation-like behavior of winds measured by GOCE (Dhadly et al., 2019).

Physics-based models of the upper atmosphere also specify the horizontal neutral winds across the globe. The Coupled-Magnetosphere-Ionosphere-Thermosphere (CMIT) Model is a physics-based model that consists of three codes: (1) the Lyon-Fedder (LFM) global magnetospheric MHD code, (2) the Rice Convection Model, and (3) the Thermosphere Ionosphere Electrodynamic General Circulation Model (TIEGCM). A detailed description of the model and the coupling procedure can be found in (Wiltberger et al. (2004) and Wang et al. (1999)). CMIT was used to study altitude variations of the horizontal wind during geomagnetic storms, validated the assumption of a shearless vertical profile of the horizontal winds in low and middle latitudes during quiet times, and showed during storm time that enhancement of momentum advection and pressure gradient forces can create large vertical sheers in the horizontal winds (Wang et al., 2008). The Global-Ionosphere Model (GITM) (Ridley et al., 2006) is another physics-based model that has been used to investigate the effects of electric potential and auroral precipitation on thermospheric wind patterns by conducting multiple simulations of a substorm event on 24 November 2012 using various combinations, revealing that GITM overestimated the magnitude of the neutral winds at GOCE altitudes (Liuzzo et al., 2015). A year-long run of GITM evaluated against nighttime neutral wind data from FPIs also indicated that GITM performs poorly at capturing spatial structure and day-to-day variability of the horizontal winds (Harding et al., 2019). While each of these models has been used to study different aspects of thermospheric horizontal winds, there is yet to be a study involving use of these models to statistically characterize thermospheric horizontal wind behavior over an extended period.

Horizontal winds have been studied to understand thermospheric climatology represented by annual/diurnal variation and semidiurnal tidal variations (Yao et al., 2015), derived from observations of neutral and electron densities from satellite data to estimate wind behavior at low latitudes (Gasperini et al., 2016), and observed with a meteor radar to investigate the efficacy of that detection method, study wind seasonality, and the reveal importance of stationary planetary waves (Korotyshkin et al., 2019). However, studies involving modeling of the horizontal winds have primarily involved validation of the Horizontal Wind Model ((Drob et al., 2015)), which recently been used to investigate the tracking of sporadic E field-aligned irregularities as a probe of thermospheric winds (Helmboldt & Taylor, 2020), and GITM being used to investigate how the magnitude and temporal variations of ion drifts affect Joule heating in relation to the vertical wind structure (Yiğit & Ridley, 2011). However, to date, the horizontal winds in GITM have not been validated extensively in any way. In order to elucidate the role horizontal winds play in thermosphere dynamics it is useful to investigate their behavior over several parameters, including magnetic local time, magnetic latitude, season, and magnetic activity, which can be represented adequately well by the auroral electrojet index (AE) (Davis and Sugiura (1966) and Weygand et al. (2014)). This approach has been done with the standard deviation of the vertical wind $\sigma(V_z)$ in Visser et al. (2019b), but has heretofore not been applied to any studies of the horizontal wind.

The purpose of this paper is to characterize the capability of GITM to model thermospheric horizontal wind behavior as a function of magnetic latitude and geomagnetic activity that has been observed in data derived from linear accelerometers. This was done by comparing GITM's outputs along the orbit track of the GOCE satellite and performing statistical analysis between the datasets after separating them into categories based on magnetic latitude, magnetic local time, and auroral electrojet index. This statistical analysis aims to reveal areas for improvement of GITM for the purposes of its continued development.

2 Methodology

Horizontal wind data along the GOCE orbit was derived from its accelerometer data: measured accelerations were used to determine a net force and torque acting on the satellite. Models described in Doornbos (2011) and Visser et al. (2018) were combined with measurements and housekeeping data to estimate the forces and torques on the spacecraft caused by the gravity gradient, magnetic attitude control, and other equipment. The residual force and torque were found by subtracting the model output from the measurement. This residual force and torque were assumed to be entirely aerodynamic, and an aerodynamic model was constructed to match it by changing the direction of the incoming flow. The wind vector was thus defined as the difference between the flow and the orbital plus co-rotation velocities. The acceleration due to drag on the spacecraft can then be written in the following form:

$$\vec{a} = -\frac{1}{2}\rho\frac{A}{m}C_D\left(\vec{v_o} - \vec{v_w}\right)^2\left(\widehat{v - v_w}\right) \quad (1)$$

where the ρ is the local thermospheric density, A is the spacecraft cross-sectional area, m is the spacecraft mass, C_D is the drag coefficient, $\vec{v_o}$ is the orbital velocity of the spacecraft, and $\vec{v_w}$ is the velocity of the thermospheric wind, which includes velocities in the along-track, cross-track, and cross-vertical directions, as well as contributions from co-rotation. It is extraordinarily difficult to separate change in ρ versus change in $v_o - v_{\mathrm{along}}$, so it is customary to assume that v_{along} is negligible given that $v_o >> v_{\mathrm{along}}$. For more information, this algorithm was described in detail in Visser et al. (2019a).

GITM was used to model horizontal winds, and was run from January to November 2013 with the conditions in Table 1.

Table 1. GITM Parameters for the Horizontal Wind Validation Study

Parameter	**Value**
Eddy Diffusion Coefficient	100
Eddy Pressure Lower	0.0050
Eddy Pressure Upper	0.0005
Photoelectron Heating Efficiency	0.02
Neutral Heating Efficiency	0.05
Thermal Conduction (Molecular)	3.6×10^{-4}
Thermal Conduction (Atomic)	5.6×10^{-4}
Thermal Conduction Power	0.69
AUSMSolver	True
CFL	0.80
Limiter	MC, 2.0
Dynamo High Lat. Boundary	45.0
Improved Ion Advection	True
Nighttime Ion B.C.s	True
Minimum TEC for Ion B.C.s	2.0

GITM is a three-dimensional, spherical, parallel code that models the thermosphere-ionosphere system using a stretched altitude grid. It allows for non-hydrostatic solutions and solves for the neutral, ion, and electron temperatures, the bulk horizontal neutral winds, the vertical velocity of the individual species, and ion and electron velocities. The code can use a dipole magnetic field, a tilted dipole, or the IGRF magnetic field with the APEX coordinate system (Richmond, 1995). The primary drivers of the thermosphere and ionosphere are solar EUV modeled by the Flare Irradiance Spectral Model (FISM) (Chamberlin et al. (2007) and Chamberlin et al. (2008)) and high-latitude electrodynamics, specified by the Weimer (2005) electrodynamic potential patterns driven by time-delayed IMF and solar wind measurements from the Advanced Composition Explorer

(ACE) satellite, and the Fuller-Rowell and Evans (1987) particle precipitation patterns driven by hemispheric power estimated by the LEO satellites operated by the National Oceanographic and Atmospheric Administration (NOAA).

As the horizontal wind in GITM was extracted along the GOCE orbit, both the GITM results and the GOCE measurements have the same 10-second temporal resolution. As the GOCE cross-track wind measurements have associated errors, some measurements may constitute outliers in the data and be too uncertain. Therefore, for wind measurements in excess of 25 m/s, if the associated error was greater than 25 m/s and the absolute value of the GOCE cross-track wind measurement was less than the associated error, the wind data were discarded.

Figure 1 shows the horizontal wind (V_x) at different times on the first six days of March 2013 along the GOCE orbit, as representative examples of GITM's performance in comparison to the GOCE data. Each of the times chosen corresponded to the time for which the largest peak in the vertical wind (not shown) was also observed in the GOCE data (Figure 5 in Visser et al. (2019b)). In each interval ($\sim$14 minutes), the the GOCE data show the horizontal wind speed rising to a crest, often featuring smaller peaks surrounding a dominant central peak. By inspection, GITM performed well in capturing the overall contour of the horizontal wind speed in each interval, especially on March 3 and March 5, though it does less well at capturing smaller features in the horizontal wind that occur over much shorter timescales than that of the central peak. The small gaps in the GOCE cross-track wind measurements on March 2 and March 4 correspond to discarded data.

By inspection, GITM performed well in about half of the times, capturing the overall contour and magnitude of the horizontal cross-track wind speed on each day, especially on March 3 and March 5, though it did less well at capturing smaller features in the wind speed that occurred over shorter timescales than that of the central peak.

We closely follow the statistical analysis of Visser et al. (2019b) and apply it to the cross-track horizontal winds. GITM V_x results were compared to GOCE V_x data in terms of their probability distributions calculated over bins with a width of 1 m/s. The means, 25th, and 50th percentiles were calculated for each distribution. We considered the effects of several controlling parameters on the GITM V_x results in comparison to the GOCE V_x data: magnetic latitude (MLAT), magnetic local time (MLT), day-of-the-year (DOY), and geomagnetic activity. We used the minute-by-minute Auroral Electroject (AE) Index to quantify geomagnetic activity. We calculated probability densities in three magnetic latitude ranges: midlatitudes (30–60°), auroral latitudes (60–80°) and polar cap latitudes (80–90°). As in Visser et al. (2019b) and Innis and Conde (2002), we further restricted each MLAT range according to the following AE bounds: AE$\leq$250, 250$<$AE$\leq$500, and AE$>$500.

In order to compare and contrast how GITM's V_x responded to different parameters and compare that responsiveness to that of the GOCE data, we again mirrored the method of Visser et al. (2019b) and distributed the data over bins of AE, MLAT, MLT, DOY, and F10.7, and plotted the 25th, 50th, and 75th percentiles of V_x. We complete our analysis with a series of implications and future steps, and describe the modeled and derived vertical winds, presenting some disagreement and challenges.

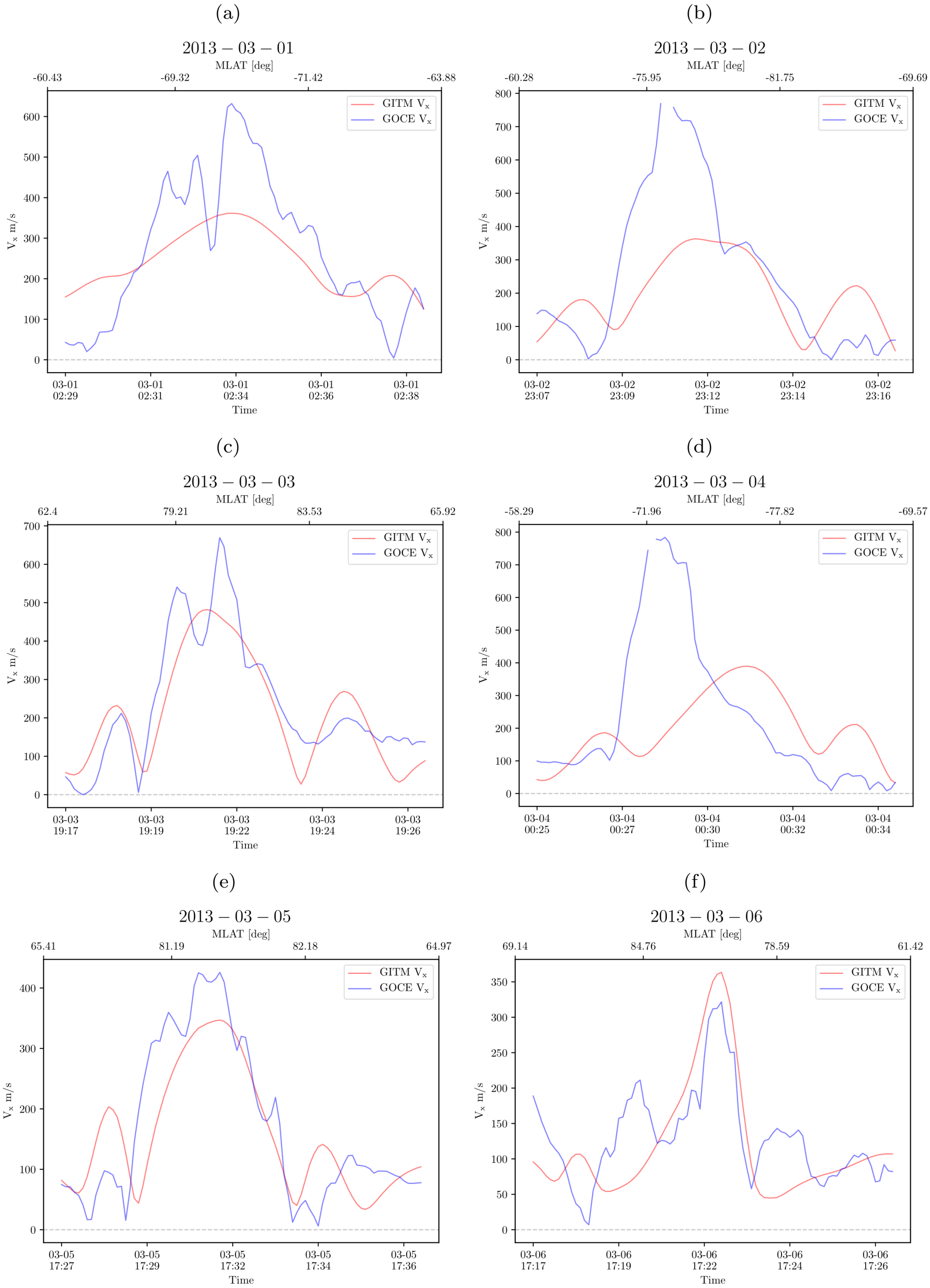

Figure 1. Time series of the 14 minutes surrounding notable large peaks in the horizontal wind V_x during the first 6 days of March 2013 for both GITM (red) and GOCE (blue). The selected times for each plot correspond to the largest peaks in the vertical wind in the GOCE data, as pointed out in Figure 5 of Visser et al. 2019. GITM performed well in all nearly cases with capturing the overall contour of the horizontal wind speed.

3 Results

The neutral winds are controlled by forces that are ordered in geographic coordinates (e.g. gradient in the day-to-night pressure and Coriolis forces) and magnetic coordinates (e.g. ion drag at high and low latitudes). Therefore, no matter which coordinate system is chosen to plot the data, there is a diurnal variation that is caused by the Earth's magnetic field rotating through the day. We have chosen to plot in magnetic coordinates to minimize the effect, but it leads to other effects, such as not having data near the magnetic equator. This is due to the choice of using a reference altitude of 100 km for the magnetic latitude, such that most of the time, GOCE (at ∼250 km) does not sample 0° magnetic latitude. With this in mind, Figures 2 and 3 show the horizontal cross-track wind speed from GITM and GOCE, as well as the difference.

During the entire time period considered, both GITM and GOCE horizontal winds showed greater speeds in the auroral region and lesser speeds in the midlatitudes, in both hemispheres and for both the ascending and descending nodes.

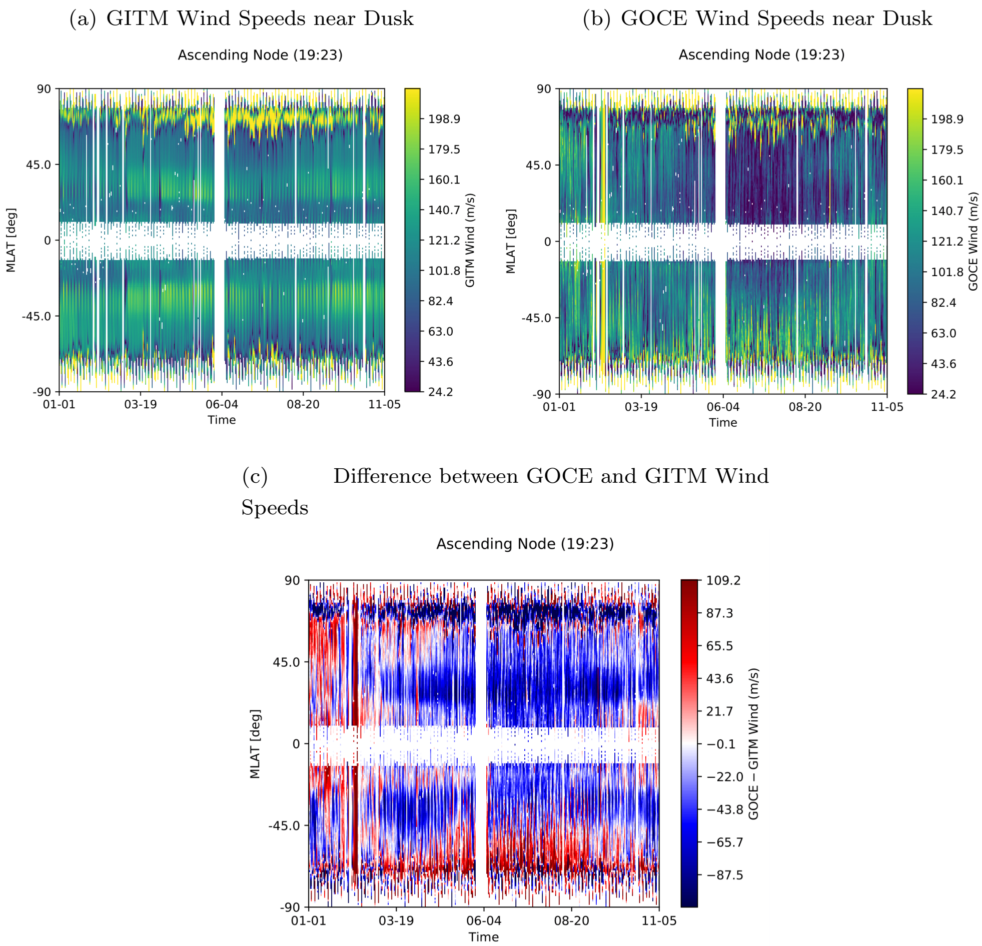

Figure 2. (a) Time series and latitude plots of the GITM (left) and GOCE (right) horizontal wind for the ascending node. (b) Time series and latitude plots of the difference between GITM and GOCE horizontal wind for the ascending node. GITM overestimated the horizontal wind speed throughout the entire time considered, especially in the midlatitudes.

By inspection, GITM's demonstrated difficulty in capturing finer latitudinal structures in the horizontal wind, and placed a morphological feature at $\pm 20° - 30°$, coincident with location of the Equatorial Ionization Anomaly (EIA). GITM also struggled with capturing some of the seasonal variation in the horizontal winds shown in the GOCE data. This is most evident in the midlatitudes for the descending node (Figure 3, near

(a) GITM Wind Speeds near Dawn

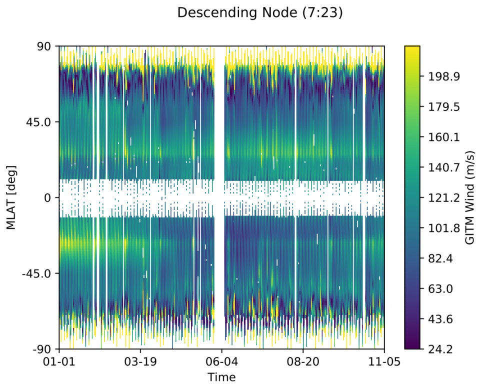

(b) GOCE Wind Speeds near Dawn

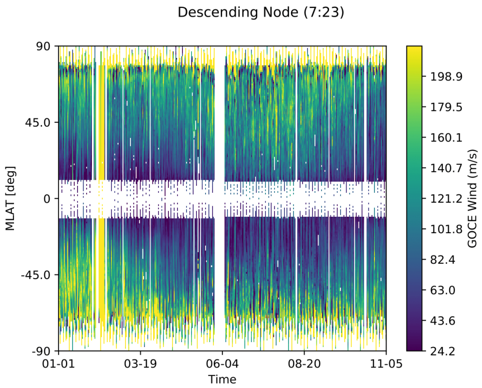

(c) Difference between GOCE and GITM Wind Speeds

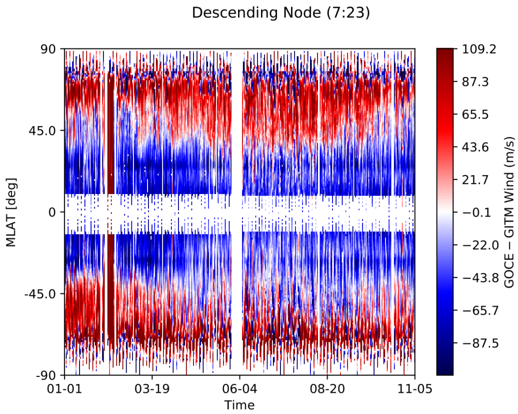

Figure 3. (a) Time series and latitude plots of the GITM (left) and GOCE (right) horizontal wind for the descending node. (b) Time series and latitude plots of the difference between GITM and GOCE horizontal wind for the descending node. GITM underestimated wind speeds in the auroral and polar latitudes, but underestimated them in the mid and low-latitudes.

dusk): The GOCE data showed that higher wind speeds begin to extend from the auroral to the equatorial region throughout the summer in the Northern Hemisphere, which GITM failed to capture, as it underestimated the winds during those times in that region. Conversely, for the ascending node (Figure 2, near dusk), during that same time period, GITM *overestimated* the horizontal winds in the same latitude region. For both the ascending and descending node throughout the entire year, GITM generally overestimated the horizontal wind speeds in the low- and midlatitudes in both hemispheres.

Additionally, Figure 2 shows that GITM overestimated the wind speed for the ascending node (dusk) most prominently during the summer, and underestimated it for the descending node (dawn). This behavior was most prominent during the height of the summer in the northern hemisphere.

Exploring V_x specifically during the first six days of March (Figure 4) shows the differences between the GITM results and GOCE winds in greater detail. GITM reproduces the diurnal variability of V_x shown in the GOCE data, but shows higher winds speeds in the EIA region, possibly due to ion drifts or ion drag that are too strong. GITM's wind

(a)

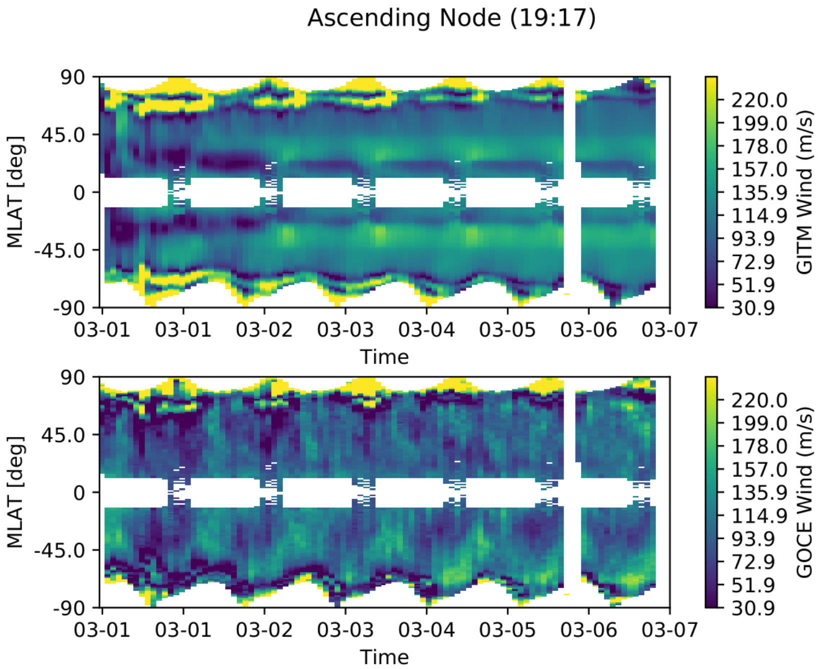

(b)

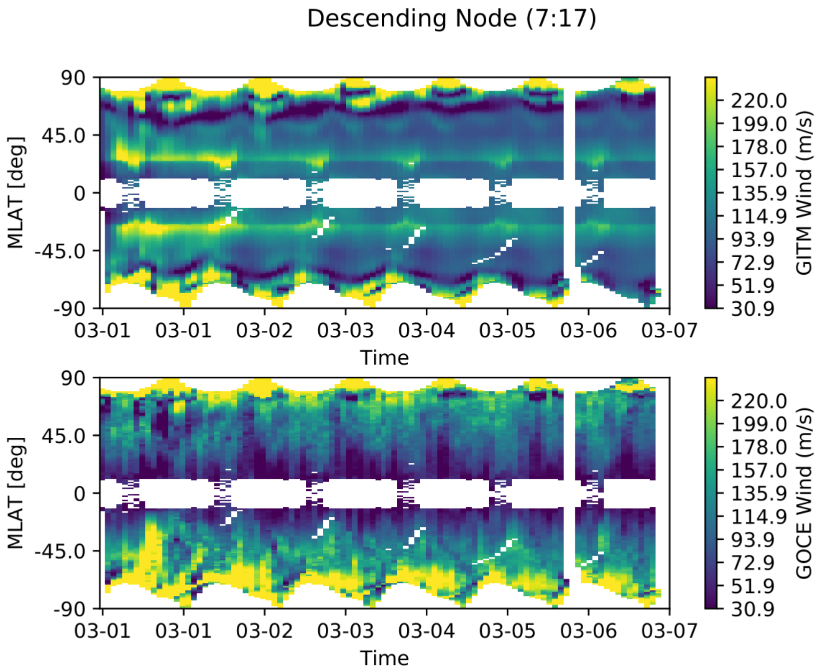

Figure 4. Time series and latitude plots of the GITM and GOCE horizontal wind for the ascending node (top) and descending node (bottom) for the first 6 days of March 2013. GITM sufficiently captures the diurnal variability shown in the GOCE data but overestimates horizontal wind speed in the EIA region.

speeds are more similar to GOCE at high latitudes in the dusk sector, but GOCE wind speeds are larger in the southern auroral zone in the dawn sector.

GOCE V_x probability distributions were compared to their GITM counterparts in each of three latitude ranges for three AE bins (Figure 5). GITM's probability distributions were generally narrower than those of GOCE outside of the polar region, most drastically in the midlatitudes, which was likely due to the constant jet coincident with the EIA. The stronger signature of diurnal variability in the GOCE data additionally shows up as wider spread in the distribution. Even though GITM's distributions were narrower in the midlatitudes, its values of mean V_x were closer to those of GOCE than in the auroral zone. This shows that GITM is more precise in the auroral latitudes but with less accuracy, and less precise in the midlatitudes but with greater overall accuracy. GITM's peak probabilities skewed towards larger V_x in comparison to GOCE in the midlatitudes, where it showed a tendency to overestimate wind speed, but skewed towards smaller V_x than GOCE in the auroral latitudes (with the exception of high activity), where it underestimated wind speeds. GITM's probabilities matched GOCE's quite well in the polar region, with the exception of during high activity, where it tended to overestimate the wind speed.

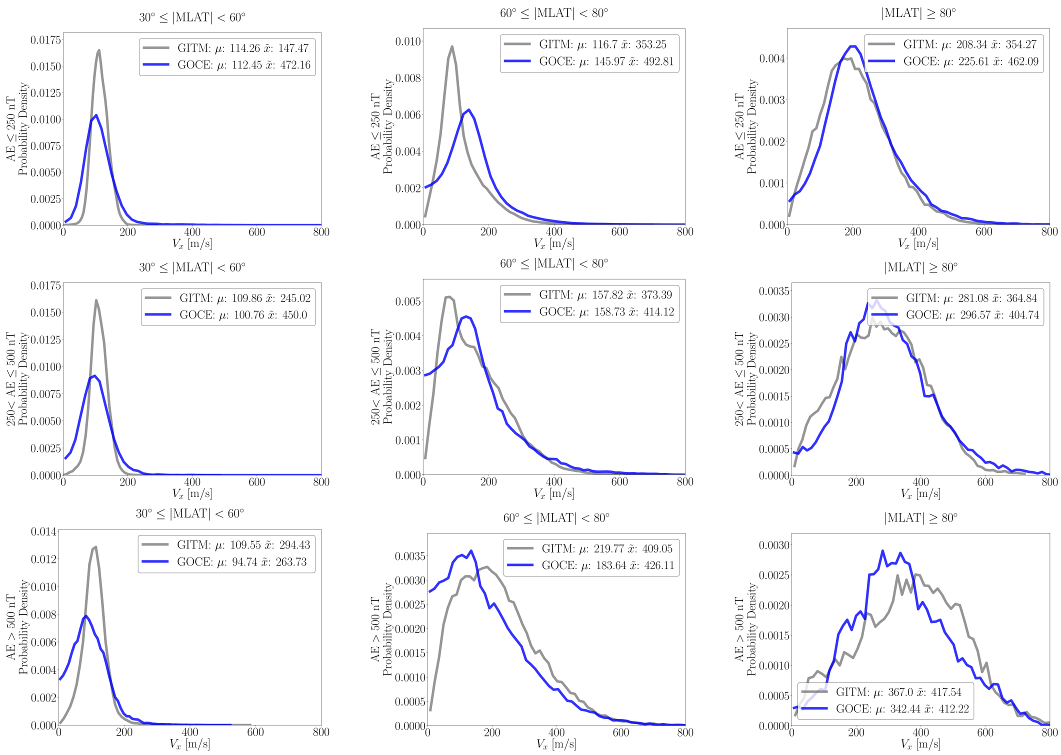

Figure 5. Probability densities of V_x for GOCE compared to GITM across the three MLAT ranges (from left to right: Mid-, auroral-, and polar-latitudes), for three different levels of geomagnetic activity described by the AE index (from top to bottom: AE $\leq$ 250, 250 $<$ AE $\leq$ 500, and AE $>$ 500). GITM's performance tended to increase with magnetic latitude and activity level.

The 10-month window chosen for this study allowed us to explore how different conditions affected the GITM results. Specifically, AE, MLT, Day of Year (DOY), and F10.7 were investigated. Because GITM was sampled at the GOCE locations and times, the number of counts of V_x per bin of the selected parameter were identical for both sets of data. The Northern and Southern Hemisphere data were combined for this analysis, except when binning the data as a function of MLT.

Figure 6 displays the dependence of V_x on the AE index for GITM in comparison to GOCE. The GOCE data show that in the low- and midlatitudes, thermospheric horizontal wind speeds decrease slightly for increasing activity level. In both these regions, GITM overestimated the wind speed, with the magnitude of the overestimation generally growing as activity level increased. GITM's wind speed overestimation was most clear in the low-latitudes, where the it grew from ~5 m/s to ~30 m/s from AE values of 50 to 1200. In contrast to the midlatitudes, where GITM's V_x values slightly decreased with activity, in the low-latitudes, GITM's V_x slightly increased with activity. In the auroral and polar zones, GITM performed much better in capturing the characteristic increase in V_x with activity level shown in the GOCE data, even though it began to overestimate the wind speed above AE=400 in both cases, growing to a difference of at least ~80 m/s at AE=1200.

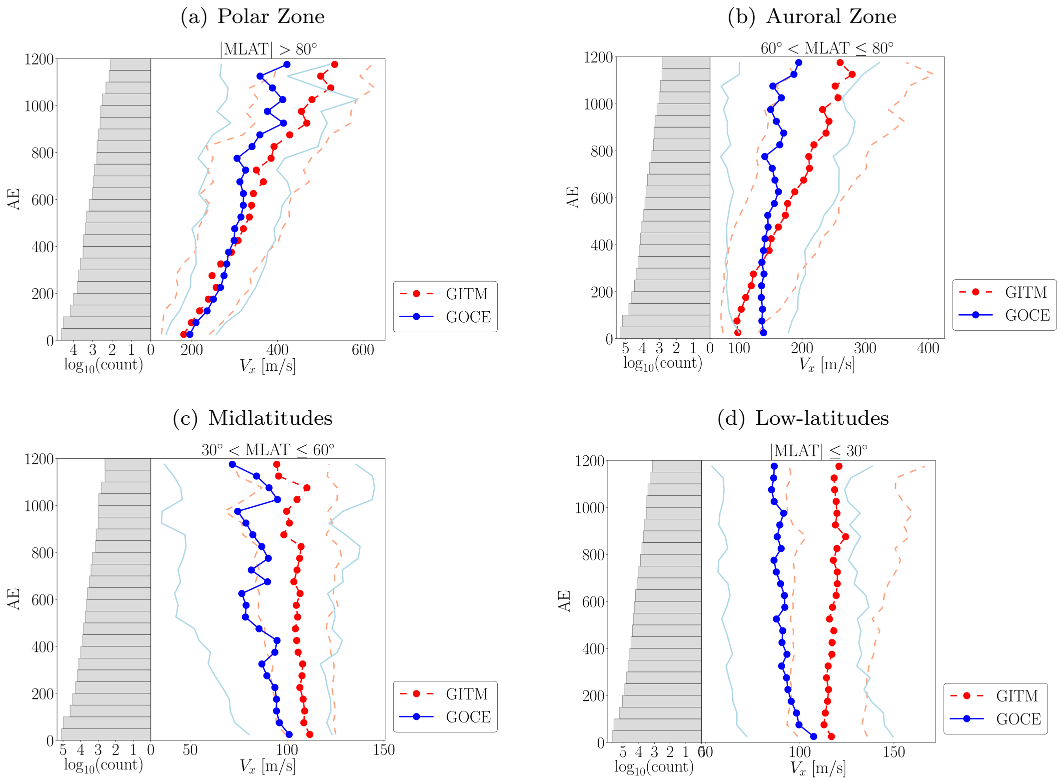

Figure 6. The 25th, 50th, and 75th percentiles of V_x per bin of AE for both the GITM and GOCE data constructing an adjacent histogram of the number of counts of data per bin. Lines corresponding to GITM are red and dashed, and lines corresponding to GOCE are blue and solid. The 25th and 75th percentiles of the GITM V_x values are in light blue, while the 50th percentile is in rich blue, marked with circles, while the 25th and 75th percentiles of the GOCE V_x values are in light red, while the 50th percentile is in rich red, also topped with circles. In the top row from left to right, the results are shown for the polar latitudes and then auroral latitudes, and in the bottom row from left to right, the results are shown for midlatitudes and the equatorial region. GITM performs best in the polar and auroral zones, with an overall tendency to overestimate the wind speed as activity increases.

Next, we consider variations with magnetic local time (Figure 7), noting characteristic troughs in the data around 7 and 19 hours, due to GOCE being in a roughly dusk-to-dawn orbit (in geographic coordinates).

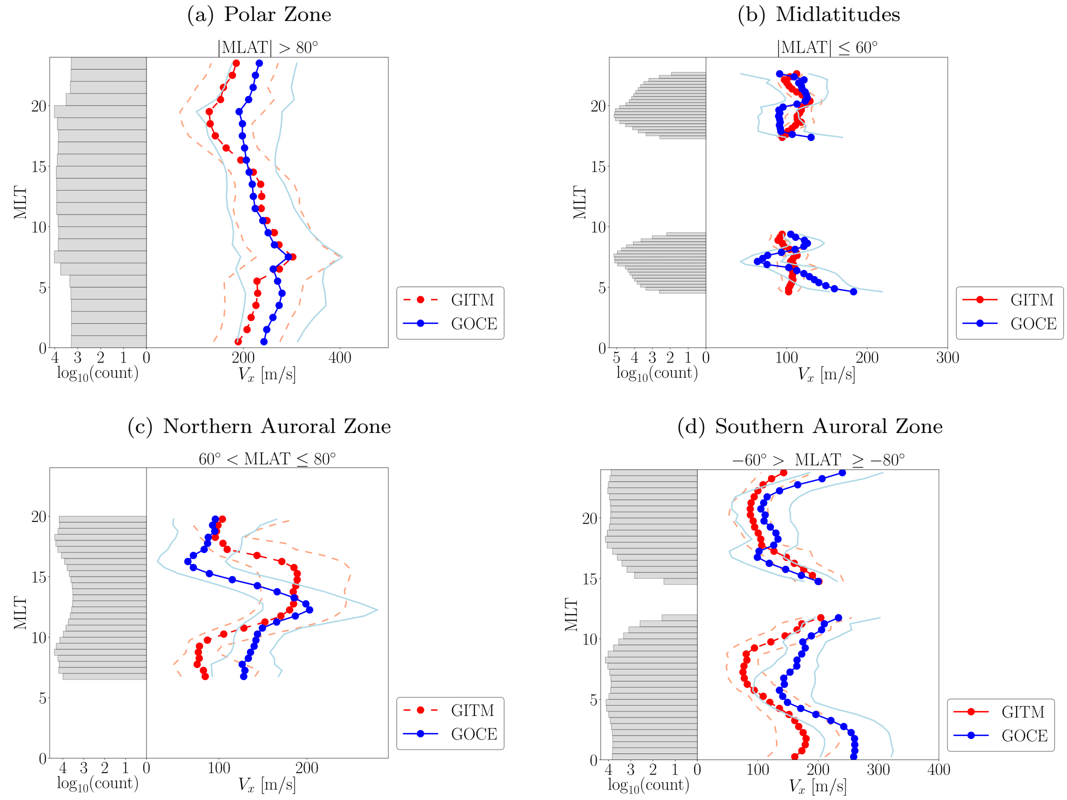

Figure 7. Top row, left to right: Percentiles (25th, 50th, and 75th) of V_x and data count, per bin of MLT over the polar region (bin width of 1 hr), auroral latitudes, and low and middle latitudes (bin width of 15 minutes). Bottom row, left to right: Percentiles (25th, 50th, and 75th) of V_x and data count, per bin of MLT index over the Northern auroral oval and Southern auroral oval, with bin widths of 30 min for both. GITM showed a tendency to underestimate the wind speed overall, and again, performed best in the polar zone.

Due to the offset between the geographic and magnetic poles, GOCE was able to sample all MLTs in the polar cap, but only near dawn and dusk at lower altitudes. In the northern auroral zone, GOCE MLT coverage was limited between mid-morning to evening, while in the southern auroral zone, GOCE covered all MLTs but excluded those around noon. In contrast to when V_x is distributed as function of AE, GITM generally underestimated V_x compared to GOCE. GITM best matched GOCE in the mid-latitudes, for which GITM's mean V_x was generally consistent with GOCE's, although with significant variability. The mismatch between GITM and GOCE was strongest in both auroral zones, with the GITM mean V_x exceeding GOCE only for 13≤MLT≤17. In the auroral zones, the greatest underestimation by GITM occurred at MLT≈0 and MLT≈7 in the southern hemisphere, where GITM's mean V_x undershot GOCE V_x by nearly 100 m/s, approximately the same magnitude by which GITM overestimated the mean V_x in the northern hemisphere near MLT=15. In the polar zone, GITM performed best for 7≤MLT≤15, where it's 25th, 50th (mean), and 75th percentiles of V_x tracked GOCE with minimal deviation. Outside of that MLT range, GITM generally underestimated V_x by ∼50 m/s.

Overall, GITM demonstrates the best performance on the dayside, and the worst performance on the nightside around midnight MLT. It may be that the solar-driven ionization, and therefore the ion drag, may be best modeled at high latitudes on the dayside.

We also compared seasonal effects in V_x separately for each hemisphere (Figure 8). Due to the reentry of GOCE in November of 2013, we are unable to extend this analysis through December of 2013. The GOCE data showed differing patterns depending on the latitude ranges considered. In the northern polar zone, GOCE showed no discernible seasonal dependence, with its values of mean V_x oscillating around $\sim$250 m/s throughout the entire time considered. GITM's values of mean V_x tracked those of GOCE very well in this region, with GITM slightly overestimating the wind speed in the days surrounding the summer solstice. GITM's 25th and 75th percentile V_x values also did not deviate much at all from those of GOCE. Contrary to the northern case, in the southern polar zone, GITM underestimated V_x in all percentiles, even though it was able to capture the overall trend in the wind speeds throughout the year. Similar to how GITM overestimated the wind most in the northern polar zone during the summer solstice, it is around that time (i.e. the southern winter solstice) that GITM underestimated the wind the southern polar zone most significantly.

In the northern auroral zone, the GOCE data showed no discernible dependency on season, with as its mean V_x clustered around $\sim$120 m/s throughout the year. GITM reproduced this behavior overall, with the slight caveat of underestimating the winds by up to $\sim$ 30 m/s between January and late February (i.e. the northern winter). GITM's 25th percentile V_x values were similarly close to those of GOCE, but GITM's 75th percentile V_x values were much higher than GOCE's between the March Equinox and just before the autumnal equinox, indicating that GITM's horizontal winds were too variable during the summer. In the southern auroral zone, the GOCE wind speeds were nearly identical to that of the northern auroral zone, except that the values of V_x were higher by tens of m/s. Here, GITM underestimated V_x in all percentiles throughout the entire time shown, and did not capture the contour of the GOCE data, instead showing a slight decline in winds speed that reaches a nadir at $\sim$100 m/s during the southern winter solstice before increasing again. GITM's underestimation can be highlighted by noting that its 75th percentile V_x values tracked the best with GOCE's mean V_x values throughout the entire year, and that its mean V_x values tracked best with GOCE's 25th percentile V_x values.

In the mid- and low-latitudes, for both hemispheres, the GOCE data showed a slight slowing of the wind across all percentiles that reached its nadir around June, before increasing slightly again. GOCE's mean V_x values clustered around 100 m/s in January for both hemispheres and decreased to $\sim$80 m/s by the summer solstice, but the following increase in wind speed leading up to the autumnal equinox was slightly more prominent in the southern hemisphere by several m/s. GITM was closest to GOCE during early January. During the rest of the year, it overestimated V_x in all percentiles compared to GOCE in both hemispheres, and its performance was less laudable in the northern hemisphere than the southern hemisphere. In the northern hemisphere, GITM did not capture the seasonal trend in V_x featuring the trough during the summer solstice, and its mean V_x values remained close to $\sim$100 m/s during the entire year. GITM performed better in the southern hemisphere, capturing the seasonality in V_x throughout the entire time shown, with its mean V_x values differing from those of GOCE by $\sim 10 - 15$ m/s outside of January and February.

We next compare the horizontal wind response to the F10.7 flux between GITM and GOCE across all latitudes (Figure 9). For the available range of F10.7 between $\sim$87 sfu and $\sim$175, the GOCE wind speed decreased in mean V_x down from $\sim$110 m/s around 90 sfu to $\sim$100 m/s around 130 sfu, before increasing to $\sim$140 m/s at 175 sfu. The GITM results did not capture this trend, with the mean V_x remaining around $\sim$120 m/s through-

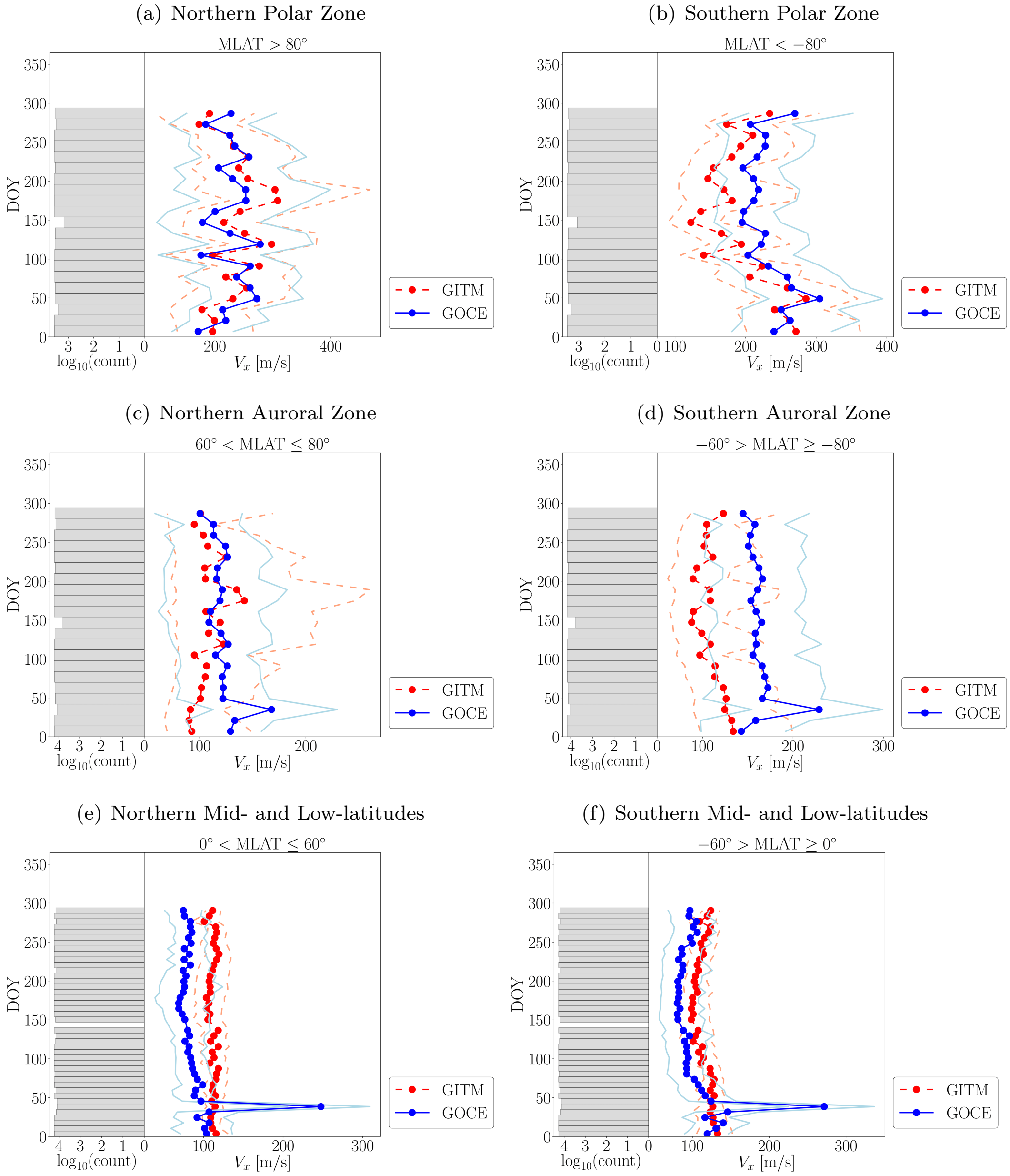

Figure 8. From the top down: Percentiles (25th, 50th, and 75th) of V_x and data count, per bin of DOY index over the Northern Hemisphere (left column) and Southern Hemisphere (right column), the polar cap an auroral oval (bin width 2 weeks), and middle latitudes (bin width 1 week). The high wind speeds in the GOCE data in mid February correspond to the bright yellow regions in Figures 1(b) and 2(b), where GOCE measured anomalously high wind speeds. The associated error with those measurements did not warrant their exclusion, despite their anomalous nature. GITM was most accurate in the northern polar and auroral zone, consistently underestimated the wind speeds in the southern polar and auroral zone, and overestimated the wind speeds in the mid- and low-latitudes.

out the entire F10.7 range. Both GITM's 25th and 75th percentile V_x values were constrained between GOCE's 25th and 75th percentile values throughout the entire F10.7

range, indicating that GITM displayed less wind variability than it should compared to the measurements.

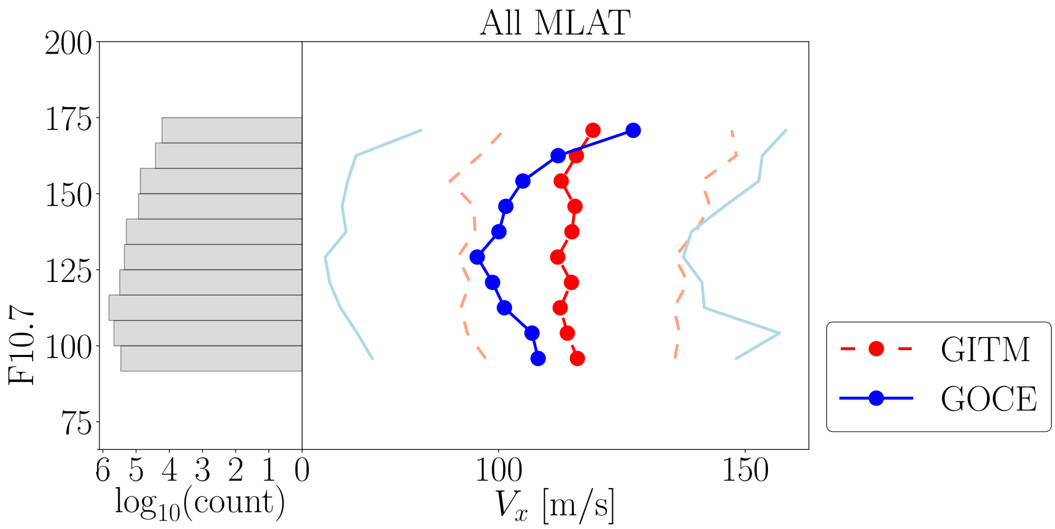

Figure 9. Percentiles (25th, 50th, and 75th) of V_x and data count, per bin of F10.7 flux, over the full MLAT range. Overall, GITM wind speeds were too high on average and not variable enough in comparison to the GOCE data.

When V_x between GITM and GOCE is compared for the ascending (dusk) and descending (dawn) nodes separately, some important differences are noticeable. For dusk (Figure 10), GITM mean V_x was consistently higher than GOCE mean V_x throughout the entire range of F10.7, except at the highest levels. GITM also modeled faster V_x values too often, as shown by its 25th percentile values being greater than those of GITM by $\sim$ 30 m/s. This behavior was not seen, however, for the 75th percentiles, for which GITM matched GOCE very well. GITM matched GOCE better for dawn (descending node) (Figure 11), following its behavior of decreasing from 90<F10.7≤135, and rising from 135<F10.7≤175. GITM mean V_x matched GOCE very well throughout the entire range of F10.7, while its 25th percentile values were slightly lower than those of GOCE, and its 75th percentile values were slightly higher than those of GOCE.

4 Conclusion and Discussion

Overall, GITM demonstrated satisfactory capability in modeling the horizontal thermospheric wind V_x in comparison to GOCE, but also shows areas for improvement. The major results are as follows:

1. Probability distributions for GITM and GOCE V_x show that GITM's performance improved as a function of MLAT, being best in the polar zone, and worst in the midlatitudes, where it seemed to have a persistent wind associated with the equatorial ionization anomalies.
2. As a function of geomagnetic activity represented by AE, GITM again performed the best in the polar and auroral zones, though it overestimated horizontal winds above AE∼400. In all MLAT regions, GITM overestimated V_x as a function of AE.
3. As a function of MLT, GITM performed the best in the polar zone near noon and worst in the auroral zones near midnight. When GITM was inaccurate compared

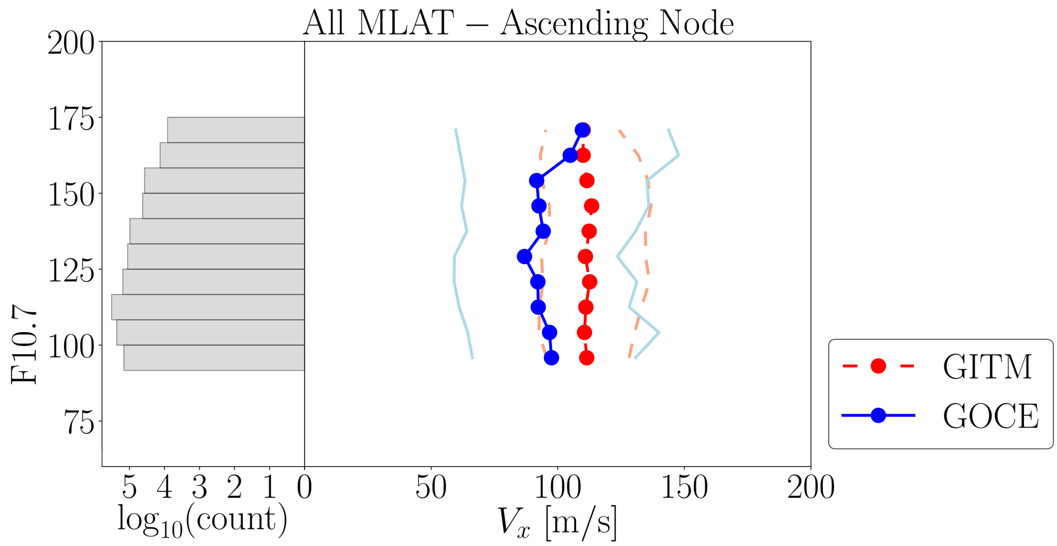

Figure 10. Percentiles (25th, 50th, and 75th) of V_x and data count, per bin of F10.7 flux, over the full MLAT range for the ascending (dusk) node. GITM overestimates the wind speeds very consistently throughout the entire F10.7 range, in all percentiles except above ∼160 sfu.

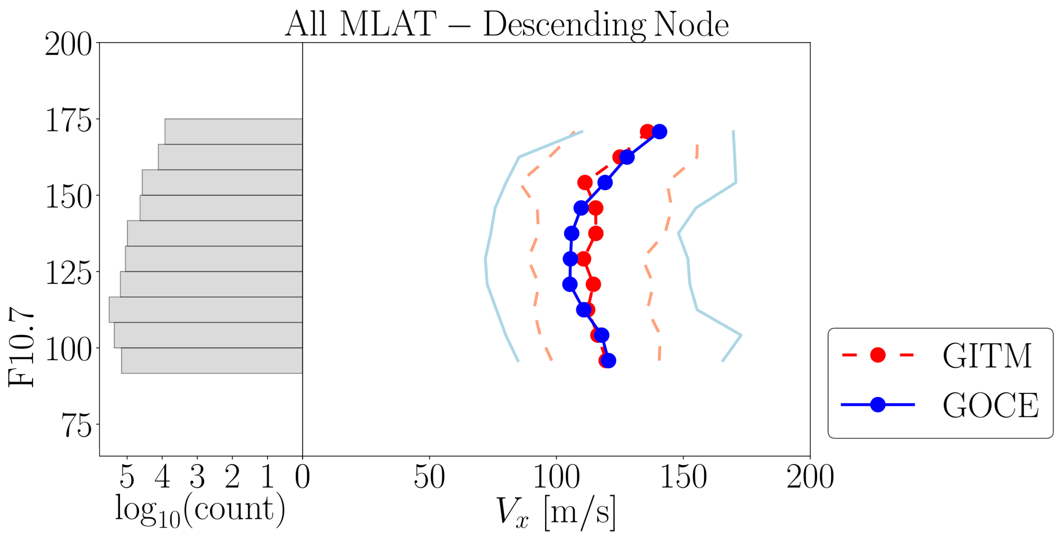

Figure 11. Percentiles (25th, 50th, and 75th) of V_x and data count, per bin of F10.7 flux, over the full MLAT range, for the descending (dawn) node. GITM matches GOCE extremely well over the entire F10.7 range.

to GOCE as a function of MLT, its tendency was to underestimate V_x more often than overestimate, with this occurring prominently for 12 >MLT< 17.

4. As a function of DOY (season), GITM performed best in the northern polar and auroral zones, and worst in the southern auroral and polar zones. Seasonality in the mid- and low-latitudes was best captured by GITM in the southern hemisphere. GITM primarily underestimated horizontal winds in the winter and overestimated them in the summer, although the amount of over and underestimation varied.

5. As a function of F10.7, GITM displayed less variability than GOCE, and overall slightly overestimated horizontal winds, except for F10.7>$\sim$ 150, where it tracked GOCE the best.
6. GITM's underestimation of winds in the summer could be an indication that ion drag could be inaccurate, which may be driven by either electron densities that are inaccurate or ion drifts that are inaccurate. This is true especially in the mid-latitudes, where there is a persistent large wind speed modeled by GITM that was at a lower amplitude in GOCE.

This study indicates that GITM's modeling of the cross-track (horizontal) wind is broadly best at higher MLAT and generally marked by underestimation and insufficient variability of V_x. This may suggest that GITM places preferential emphasis on high-latitude drivers and needs further improvements in its handling of quiet-time conditions, as well as modeling of the seasonality of the diurnal tide, which displays amplitudes 2-3 times larger at equinoxes compared to solstices (Lu et al., 2011). Addressing these concerns may improve GITM's ability to capture seasonality, especially at the mid- and low-latitudes. Additional work includes investigating how improved modeling of viscosity and temperature can aid in GITM's modeling of thermospheric winds, as well as a follow-up study covering a wider period of time and incorporating both data from satellites and ground-based FPIs.

4.1 Vertical Winds

Vertical winds are additionally of interest as a subject of study, as upward motion in the thermosphere is typically accompanied by horizontal divergence of air higher in the thermosphere, and horizontal convergence of air lower in the thermosphere, with the vertical velocity being inversely proportional to the density and directly proportional to the pressure gradient (Rishbeth & Müller-Wodarg, 1999). It is conventional to assume a hydrostatic atmosphere, which results in the vertical wind emerging as a consequence of redistributed pressure levels, where it acts as a crucial component of adiabatic cooling (Hsu et al., 2014). GITM simulations have shown that vertical pressure gradient force can locally exceed the gravity force by 25% during strong driving, creating non-hydrostatic conditions, generating a disturbance transported from lower altitudes to higher altitudes through an acoustic wave, which can drive vertical wind perturbations to 150 m/s at 300 km, and raise the neutral density at high altitudes by more than 100% (Deng & Ridley, 2006). GITM simulations have also indicated that heating above 150 km is a primary source for a large increase of the average vertical velocity (40 m/s) at higher altitudes (Deng et al., 2011). Vertical winds exhibit increased variability and higher peak velocities with increasing magnetic latitude (Spencer et al., 1982). In the northern polar cap, the vertical wind velocities can routinely reach maximums of approximately 50 m/s (Ishii et al., 2004), while downward velocities in excess of 100 m/s have been measured at Southern high-latitudes (Anderson et al., 2011). It remains, however, unclear, what mechanisms are primarily responsible for driving the different levels of the vertical wind at various latitudes and altitudes.

Figure 12 shows a comparison between GITM and GOCE vertical winds for 10 months. The differences between GITM and GOCE are significant, most clearly manifesting in GITM modeling comparatively slow wind speeds in the upward direction, and with global uniformity and little variability.

As the behavior between GITM and GOCE the two shows strong disagreement, and the following should be addressed:

1. GITM is unable to reproduce the GOCE data that show higher upward motion in northern hemisphere and downward motion in the southern hemisphere. Not only does GITM not show this behavior whatsoever, but it shows a nodal depen-

(a)

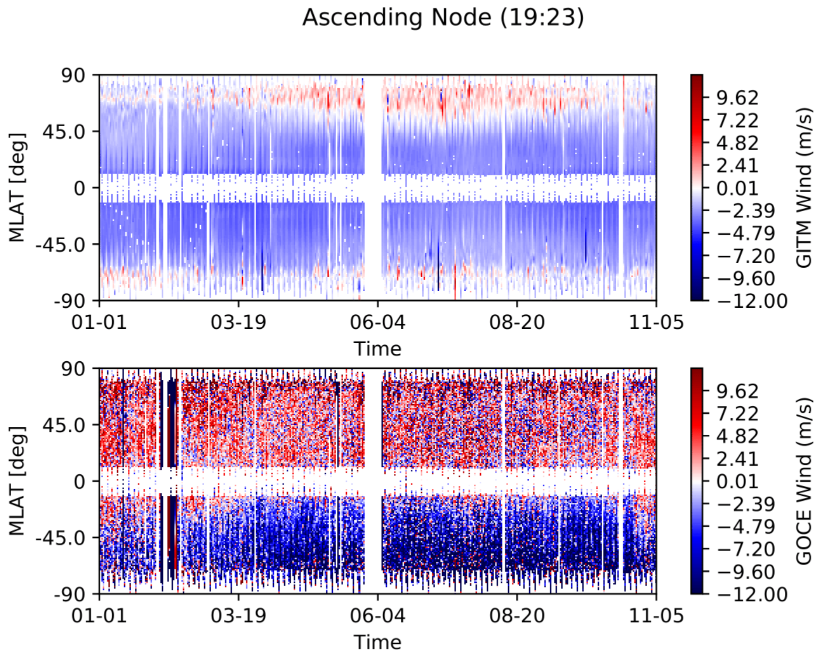

(b)

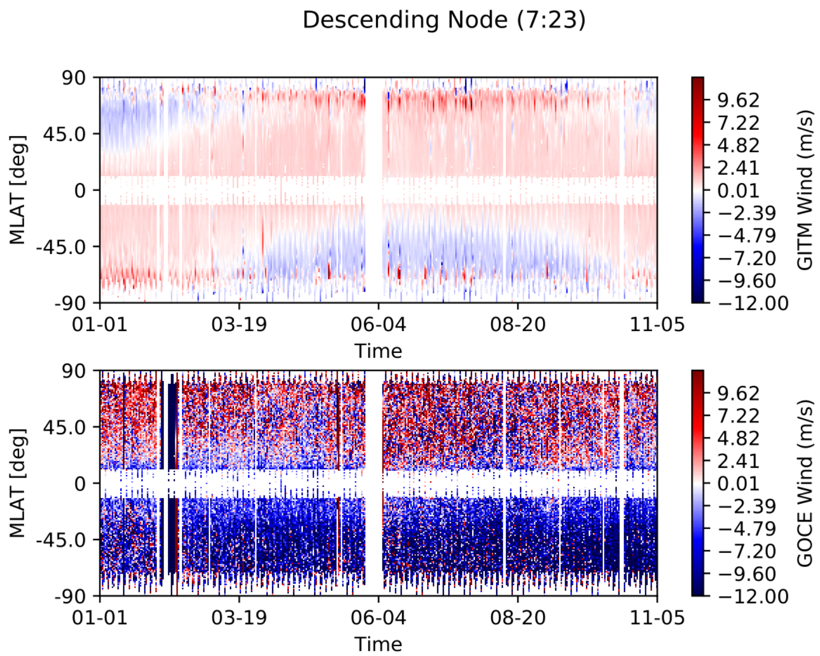

Figure 12. Time series and latitude plots of the GITM and GOCE vertical wind for the ascending node (top) and descending node (bottom) for the entirety of available data for 2013. GITM vertical winds are primarily downward for the ascending node and primarily upwards for the descending node, a dichotomy not seen in the GOCE data. Additionally, the GITM vertical wind speeds are notably slower than those of GOCE.

dency: GITM winds are primarily downward for the ascending node and primarily upward for the descending node.

2. GITM results show too little variability in the vertical wind. This is most drastic in the northern hemisphere, where the GOCE data shows a random distribution of faster upward winds approaching 10 m/s. This behavior is nonexistent in the GITM results.
3. The lack of variability in the GITM results compared to the GOCE data raises questions about GITM's assumptions regarding sources of energy input. In GITM, and it is assumed in the thermosphere, the main source of energy input variability is in the auroral zone. If there is another source of energy input, such as waves from the lower atmosphere (Holton, 1982) that are known to have thermal effects on planetary atmospheres (Müller-Wodarg et al., 2019), that can drive such strong variability in the vertical winds, it is not included in any model of the thermosphere.
4. It is unclear if the vertical winds measured by GOCE are correct to begin with. The hemispherical differences warrant investigation and comparison to ground-based data.

While it is possible that GITM could be underestimating vertical wind speeds overall, and especially the variability at high latitudes due to auroral forcing, it is unclear whether or not the GOCE vertical winds are an accurate representation of the vertical winds. More measurements of the vertical winds at all latitudes and seasons are needed to address these discrepancies. Furthermore, comparisons to whole atmosphere models such as WACCM-X (H.-L. Liu et al. (2010) and H.-L. Liu et al. (2018)) or GAIA (Jin et al., 2011) may demonstrate whether there exists significant wave driving from the lower atmosphere that could guarantee variability of vertical winds to ± 15 m/s at middle and low latitudes.

Acknowledgments

This work was supported by the joint NSF-NASA Space Weather with Quantified Uncertainties program under NASA grant: 80NSSC20K1581. We additionally acknowledge use of the World Data Center for Geomagnetism to obtain AE Index measurements for the year of 2013 (http://wdc.kugi.kyoto-u.ac.jp/dstae/index.html). The data and code used for this study is housed on the DeepBlue archive of the University of Michigan: https://doi.org/10.7302/wzc1-vc88. Data is also accessible on Google Drive: https://drive.google.com/drive/u/1/folders/1f7lVxGMfgf_zjwQoJaKOItU1dM3ifLGd

References

Anderson, C. T., Davies, M., Conde, M., Dyson, P., & Kosch, M. J. (2011). Spatial sampling of the thermospheric vertical wind field at auroral latitudes. *J. Geophys. Res.*, *116*(A06320).

Billett, D. D., McWilliams, K. A., & Conde, M. G. (2020). Colocated observations of the e and f region thermosphere during a substorm. *Journal of Geophysical Research: Space Physics*, *125*(11), e2020JA028165. Retrieved from `https://agupubs.onlinelibrary.wiley.com/doi/abs/10.1029/2020JA028165` (e2020JA028165 10.1029/2020JA028165) doi: https://doi.org/10.1029/2020JA028165

Biondi, M. A. (1984). Measured vertical motion and converging and diverging horizontal flow of the midlatitude thermosphere. *Geophysical Research Letters*, *11*, 84–87.

Biondi, M. A., & Sipler, D. P. (1985). Horizontal and vertical winds and temperatures in the equatorial thermosphere: Measurements from natal, brazil during august–september 1982. *Planetary and Space Science*, *33*(7), 817-823. Retrieved from `https://www.sciencedirect.com/science/article/pii/`

0032063385900352 doi: https://doi.org/10.1016/0032-0633(85)90035-2
Bowman, M. R., GIbson, A. J., & Sandford, M. C. W. (1969, Feb 01). Atmospheric sodium measured by a tuned laser radar. *Nature*, *221*(5179), 456-457. Retrieved from https://doi.org/10.1038/221456a0 doi: 10.1038/221456a0
Burns, A. G., Killeen, T. L., & Roble, R. G. (1989). Causes of changes in composition calculated using a thermospheric general circulation model. *J. Geophys. Res.*, *94*, 3670–3686.
Burns, A. G., Killeen, T. L., & Roble, R. G. (1991). A simulation of the thermospheric composition changes during an impulse storm. *J. Geophys. Res.*, *96*, 14153–14167.
Ceplecha, Z., Borovička, J., Elford, W. G., ReVelle, D. O., Hawkes, R. L., Porubčan, V., & Šimek, M. (1998, Sep 01). Meteor phenomena and bodies. *Space Science Reviews*, *84*(3), 327-471. Retrieved from https://doi.org/10.1023/A:1005069928850 doi: 10.1023/A:1005069928850
Chamberlin, P. C., Woods, T. N., & Eparvier, F. G. (2007). Flare irradiance spectral model (fism): Daily component algorithms and results. *Space Weather*, *5*(7). Retrieved from https://agupubs.onlinelibrary.wiley.com/doi/abs/10.1029/2007SW000316 doi: https://doi.org/10.1029/2007SW000316
Chamberlin, P. C., Woods, T. N., & Eparvier, F. G. (2008). Flare irradiance spectral model (fism): Flare component algorithms and results. *Space Weather*, *6*(5). Retrieved from https://agupubs.onlinelibrary.wiley.com/doi/abs/10.1029/2007SW000372 doi: https://doi.org/10.1029/2007SW000372
Chau, J. L., & Clahsen, M. (2019). Empirical phase calibration for multistatic specular meteor radars using a beamforming approach. *Radio Science*, *54*(1), 60-71. Retrieved from https://agupubs.onlinelibrary.wiley.com/doi/abs/10.1029/2018RS006741 doi: https://doi.org/10.1029/2018RS006741
Chu, X., Yu, Z., Gardner, C. S., Chen, C., & Fong, W. (2011). Lidar observations of neutral fe layers and fast gravity waves in the thermosphere (110–155 km) at mcmurdo (77.8°s, 166.7°e), antarctica. *Geophysical Research Letters*, *38*(23). Retrieved from https://agupubs.onlinelibrary.wiley.com/doi/abs/10.1029/2011GL050016 doi: https://doi.org/10.1029/2011GL050016
Conde, M., & Smith, R. W. (1998). Spatial structure in the thermospheric horizontal wind above poker flat, alaska, during solar minimum. *Journal of Geophysical Research: Space Physics*, *103*(A5), 9449-9471. Retrieved from https://agupubs.onlinelibrary.wiley.com/doi/abs/10.1029/97JA03331 doi: https://doi.org/10.1029/97JA03331
Dandenault, P. B. (2018). Mentat: A new wind model for earth's thermosphere. *Journal of Geophysical Research: Space Physics*, *123*(8), 7124-7147. Retrieved from https://agupubs.onlinelibrary.wiley.com/doi/abs/10.1029/2018JA025551 doi: https://doi.org/10.1029/2018JA025551
Davis, T. N., & Sugiura, M. (1966). Auroral electrojet activity index ae and its universal time variations. *Journal of Geophysical Research (1896-1977)*, *71*(3), 785-801. Retrieved from https://agupubs.onlinelibrary.wiley.com/doi/abs/10.1029/JZ071i003p00785 doi: https://doi.org/10.1029/JZ071i003p00785
Deng, Y., Fuller-Rowell, T. J., Akmaev, R. A., & Ridley, A. J. (2011). Impact of the altitudinal joule heating distribution on the thermosphere. *Journal of Geophysical Research: Space Physics*, *116*(A05313).
Deng, Y., & Ridley, A. J. (2006). Dependence of neutral winds on convection e-field, solar euv, and auroral particle precipitation at high latitudes. *Journal of Geophysical Research*, *111*.
Dhadly, M. S., Emmert, J. T., Drob, D. P., Conde, M. G., Aruliah, A., Doornbos, E., ... Ridley, A. J. (2019). Hl-twim empirical model of high-latitude upper thermospheric winds. *Journal of Geophysical Research: Space Physics*, *124*(12), 10592-10618. Retrieved from https://agupubs.onlinelibrary

.wiley.com/doi/abs/10.1029/2019JA027188 doi: https://doi.org/10.1029/2019JA027188

Doornbos, E. (2011). Thermospheric density and wind determination from satellite dynamics (ph.d. thesis). *Delft University of Technology, Delft, The Netherlands*.

Drob, D. P., Emmert, J. T., Crowley, G., Picone, J. M., Shepherd, G. G., Skinner, W., ... Vincent, R. A. (2008). An empirical model of the earth's horizontal wind fields: Hwm07. *Journal of Geophysical Research: Space Physics*, *113*(A12). Retrieved from https://agupubs.onlinelibrary.wiley.com/doi/abs/10.1029/2008JA013668 doi: https://doi.org/10.1029/2008JA013668

Drob, D. P., Emmert, J. T., Meriwether, J. W., Makela, J. J., Doornbos, E., Conde, M., ... Klenzing, J. H. (2015). An update to the horizontal wind model (hwm): The quiet time thermosphere. *Earth and Space Science*, *2*, 301-319.

fang Du, L., tao Yang, G., hong Wang, J., Yue, C., & xiang Chen, L. (2017). Implementing a wind measurement doppler lidar based on a molecular iodine filter to monitor the atmospheric wind field over beijing. *Journal of Quantitative Spectroscopy and Radiative Transfer*, *188*, 3-11. Retrieved from https://www.sciencedirect.com/science/article/pii/S0022407316300486 (Advances in Atmospheric Light Scattering: Theory and Remote Sensing Techniques) doi: https://doi.org/10.1016/j.jqsrt.2016.07.013

Floberghagen, R., Fehringer, M., Lamarre, D., Muzi, D., Frommknecht, B., Steiger, C., ... da Costa, A. (2011). Mission design, operation and exploitation of the gravity field and steady-state ocean circulation explorer mission. *Journal of Geodesy*, *85*, 749-758. doi: https://doi.org/10.007/s00190-011-0498-3

Fujii, J., Nakamura, T., Tsuda, T., & Shiokawa, K. (2004). Comparison of winds measured by mu radar and fabry–perot interferometer and effect of oi5577 airglow height variations. *Journal of Atmospheric and Solar-Terrestrial Physics*, *66*(6), 573-583. Retrieved from https://www.sciencedirect.com/science/article/pii/S1364682604000215 (Dynamics and Chemistry of the MLT Region - PSMOS 2002 International Symposium) doi: https://doi.org/10.1016/j.jastp.2004.01.010

Fuller-Rowell, T. J., & Evans, D. S. (1987). Height-integrated pedersen and hall conductivity patterns inferred from the tiros-noaa satellite data. *Journal of Geophysical Research: Space Physics*, *92*(A7), 7606-7618. Retrieved from https://agupubs.onlinelibrary.wiley.com/doi/abs/10.1029/JA092iA07p07606 doi: https://doi.org/10.1029/JA092iA07p07606

Gao, Q., Chu, X., Xue, X., Dou, X., Chen, T., & Chen, J. (2015). Lidar observations of thermospheric na layers up to 170 km with a descending tidal phase at lijiang (26.7°n, 100.0°e), china. *Journal of Geophysical Research: Space Physics*, *120*(10), 9213-9220. Retrieved from https://agupubs.onlinelibrary.wiley.com/doi/abs/10.1002/2015JA021808 doi: https://doi.org/10.1002/2015JA021808

Gardner, J., Broadfoot, A., McNeil, W., Lai, S., & Murad, E. (1999). Analysis and modeling of the glo-1 observations of meteoric metals in the thermosphere. *Journal of Atmospheric and Solar-Terrestrial Physics*, *61*(7), 545-562. Retrieved from https://www.sciencedirect.com/science/article/pii/S1364682699000139 doi: https://doi.org/10.1016/S1364-6826(99)00013-9

Gasperini, F., Forbes, J. M., Doornbos, E. N., & Bruinsma, S. L. (2015). Wave coupling between the lower and middle thermosphere as viewed from timed and goce. *Journal of Geophysical Research: Space Physics*, *120*(7), 5788-5804. Retrieved from https://agupubs.onlinelibrary.wiley.com/doi/abs/10.1002/2015JA021300 doi: https://doi.org/10.1002/2015JA021300

Gasperini, F., Forbes, J. M., Doornbos, E. N., & Bruinsma, S. L. (2016). Synthetic thermosphere winds based on champ neutral and plasma density measurements. *Journal of Geophysical Research: Space Physics*, *121*(4), 3699-3721.

Retrieved from https://agupubs.onlinelibrary.wiley.com/doi/abs/10.1002/2016JA022392 doi: https://doi.org/10.1002/2016JA022392

Guo, J.-P., Deng, Y., Zhang, D.-H., Lu, Y., Sheng, C., & Zhang, S.-R. (2018). The effect of subauroral polarization streams on ionosphere and thermosphere during the 2015 st. patrick's day storm: Global ionosphere-thermosphere model simulations. *Journal of Geophysical Research: Space Physics*, *123*(3), 2241-2256. Retrieved from https://agupubs.onlinelibrary.wiley.com/doi/abs/10.1002/2017JA024781 doi: https://doi.org/10.1002/2017JA024781

Harding, B. J., Ridley, A. J., & Makela, J. J. (2019). Thermospheric weather as observed by ground-based fpis and modeled by gitm. *Journal of Geophysical Research: Space Physics*, *124*(2), 1307-1316. Retrieved from https://agupubs.onlinelibrary.wiley.com/doi/abs/10.1029/2018JA026032 doi: https://doi.org/10.1029/2018JA026032

Hedin, A. E., Biondi, M. A., Burnside, R. G., Hernandez, G., Johnson, R. M., Killeen, T. L., ... Virdi, T. S. (1991). Revised global model of thermosphere winds using satellite and ground-based observations. *Journal of Geophysical Research: Space Physics*, *96*(A5), 7657-7688. Retrieved from https://agupubs.onlinelibrary.wiley.com/doi/abs/10.1029/91JA00251 doi: https://doi.org/10.1029/91JA00251

Hedin, A. E., Spencer, N. W., & Killeen, T. L. (1988). Empirical global model of upper thermosphere winds based on atmosphere and dynamics explorer satellite data. *Journal of Geophysical Research: Space Physics*, *93*(A9), 9959-9978. Retrieved from https://agupubs.onlinelibrary.wiley.com/doi/abs/10.1029/JA093iA09p09959 doi: https://doi.org/10.1029/JA093iA09p09959

Helmboldt, J. F., & Taylor, G. B. (2020). All-sky tracking of sporadic field-aligned irregularities as a novel probe of thermospheric winds. *Earth and Space Science*, *7*(4), e2019EA000867. Retrieved from https://agupubs.onlinelibrary.wiley.com/doi/abs/10.1029/2019EA000867 (e2019EA000867 10.1029/2019EA000867) doi: https://doi.org/10.1029/2019EA000867

Holton, J. R. (1982). The role of gravity wave induced drag and diffusion in the momentum budget of the mesosphere. *Journal of Atmospheric Sciences*, *39*(4), 791 - 799. Retrieved from https://journals.ametsoc.org/view/journals/atsc/39/4/1520-0469_1982_039_0791_trogwi_2_0_co_2.xml doi: 10.1175/1520-0469(1982)039⟨0791:TROGWI⟩2.0.CO;2

Hsu, V. W., Thayer, J. P., Lei, J., & Wang, W. (2014). Formation of the equatorial thermosphere anomaly trough: Local time and solar cycle variations. *J. Geophys. Res.: Sp. Phys.*, *119*.

Innis, J. L., & Conde, M. (2002). High-latitude thermospheric vertical wind activity from dynamics explorer 2 wind and temperature spectrometer observations: Indications of a source region for polar cap gravity waves. *J. Geophys. Res.: Sp. Phys.*, *107*, 1172.

Ishii, M., Kubota, M., Conde, M., Smith, R. W., & Krynicki, M. (2004). Vertical wind distribution in the polar thermosphere during horizontal e region experiment (hex) campaign. *J. Geophys. Res.*, *109*(A12311).

Jiang, G., Xu, J., Wang, W., Yuan, W., Zhang, S., Yu, T., ... Li, Q. (2018). A comparison of quiet time thermospheric winds between fpi observations and model calculations. *Journal of Geophysical Research: Space Physics*, *123*(9), 7789-7805. Retrieved from https://agupubs.onlinelibrary.wiley.com/doi/abs/10.1029/2018JA025424 doi: https://doi.org/10.1029/2018JA025424

Jin, H., Miyoshi, Y., Fujiwara, H., Shinagawa, H., Terada, K., Terada, N., ... Saito, A. (2011). Vertical connection from the tropospheric activities to the ionospheric longitudinal structure simulated by a new earth's whole atmosphere-ionosphere coupled model. *Journal of Geophysical Research: Space Physics*, *116*(A1). Retrieved from https://agupubs.onlinelibrary.wiley.com/doi/

abs/10.1029/2010JA015925 doi: https://doi.org/10.1029/2010JA015925

Johnson, F. S., Hanson, W. B., Coley, W. R., Carignan, G. R., & Spencer, N. W. (1995). Gravity waves near 300 km over the polar cap. *J. Geophys. Res.*, *100*(23), 23,993–24,002.

Khattatov, B. V., Yubin, V. A., Geller, M. A., Hays, P. B., & Vincent, R. A. (1997). Diurnal migrating tide as seen by the high-resolution doppler imager/uars: 1. monthly mean global meridional winds. *Journal of Geophysical Research: Atmospheres*, *102*(D4), 4405-4422. Retrieved from https://agupubs.onlinelibrary.wiley.com/doi/abs/10.1029/96JD03655 doi: https://doi.org/10.1029/96JD03655

Killeen, T. L., Nardi, B., Purcell, P. N., Roble, R. G., Fuller-Rowell, T. J., & Rees, D. (1992). *Geophysical Research Letter*, *19*(11), 1093-1096.

Killeen, T. L., Wu, Q., Solomon, S. C., Ortland, D. A., Skinner, W. R., Niciejewski, R. J., & Gell, D. A. (2006). Timed doppler interferometer: Overview and recent results. *Journal of Geophysical Research: Space Physics*, *111*(A10). Retrieved from https://agupubs.onlinelibrary.wiley.com/doi/abs/10.1029/2005JA011484 doi: https://doi.org/10.1029/2005JA011484

Korotyshkin, D., Merzlyakov, E., Sherstyukov, O., & Valiullin, F. (2019). Mesosphere/lower thermosphere wind regime parameters using a newly installed skiymet meteor radar at kazan (56°n, 49°e). *Advances in Space Research*, *63*(7), 2132-2143. Retrieved from https://www.sciencedirect.com/science/article/pii/S0273117718309475 doi: https://doi.org/10.1016/j.asr.2018.12.032

Liu, A. Z., Guo, Y., Vargas, F., & Swenson, G. R. (2016). First measurement of horizontal wind and temperature in the lower thermosphere (105–140 km) with a na lidar at andes lidar observatory. *Geophysical Research Letters*, *43*(6), 2374-2380. Retrieved from https://agupubs.onlinelibrary.wiley.com/doi/abs/10.1002/2016GL068461 doi: https://doi.org/10.1002/2016GL068461

Liu, H., Doornbos, E., & Nakashima, J. (2016). Thermospheric wind observed by goce: Wind jets and seasonal variations. *Journal of Geophysical Research: Space Physics*, *121*(7), 6901-6913. Retrieved from https://agupubs.onlinelibrary.wiley.com/doi/abs/10.1002/2016JA022938 doi: https://doi.org/10.1002/2016JA022938

Liu, H.-L., Bardeen, C. G., Foster, B. T., Lauritzen, P., Liu, J., Lu, G., ... Wang, W. (2018). Development and validation of the whole atmosphere community climate model with thermosphere and ionosphere extension (waccm-x 2.0). *Journal of Advances in Modeling Earth Systems*, *10*(2), 381-402. Retrieved from https://agupubs.onlinelibrary.wiley.com/doi/abs/10.1002/2017MS001232 doi: https://doi.org/10.1002/2017MS001232

Liu, H.-L., Foster, B. T., Hagan, M. E., McInerney, J. M., Maute, A., Qian, L., ... Oberheide, J. (2010). Thermosphere extension of the whole atmosphere community climate model. *Journal of Geophysical Research: Space Physics*, *115*(A12). Retrieved from https://agupubs.onlinelibrary.wiley.com/doi/abs/10.1029/2010JA015586 doi: https://doi.org/10.1029/2010JA015586

Liuzzo, L. R., Ridley, A. J., Perlongo, N. J., Mitchell, E. J., Conde, M., Hampton, D. L., ... Nicolls, M. J. (2015). High-latitude ionospheric drivers and their effects on wind patterns in the thermosphere. *J. Geophys. Res.: Sp. Phys.*, *120*, 715–735.

Lu, X., Liu, A. Z., Oberheide, J., Wu, Q., Li, T., Li, Z., ... Franke, S. J. (2011). Seasonal variability of the diurnal tide in the mesosphere and lower thermosphere over maui, hawaii (20.7n, 156.3w). *Journal of Geophysical Research: Atmospheres*, *116*(D17). Retrieved from https://agupubs.onlinelibrary.wiley.com/doi/abs/10.1029/2011JD015599 doi: https://doi.org/10.1029/2011JD015599

Makela, J., Meriwether, J. W., Ridley, A. J., Ciocca, M., & Castellez, M. W. (2012). Large-scale measurements of thermospheric dynamics with a multi-site fabry-perot interferometer network: Overview of plans and results from midlatitude measurements. *International Journal of Geophysics*, *2012*. doi: https://doi.org/10.1155/2012/872140

Makela, J. J., Fisher, D. J., Meriwether, J. W., Buriti, R. A., & Medeiros, A. F. (2013). Near-continual ground-based nighttime observations of thermospheric neutral winds and temperatures over equatorial brazil from 2009 to 2012. *Journal of Atmospheric and Solar-Terrestrial Physics*, *103*, 94-102.

Martinis, C., Meriwether, J., Niciejewski, R., Biondi, M. A., Fesen, C., & Mendillo, M. (2001). Zonal neutral winds at equatorial and low latitudes. *Journal of Atmospheric and Solar-Terrestrial Physics*, *63*, 1559-1569.

Meriwether, J. W., Makela, J. J., Huang, Y., Fisher, D. J., Buriti, R. A., Medeiros, A. F., & Takahashi, H. (2011). Climatology of the nighttime equatorial thermospheric winds and temperatures over brazil near solar minimum. *Journal of Geophysical Research: Space Physics*, *116*(A4). Retrieved from `https://agupubs.onlinelibrary.wiley.com/doi/abs/10.1029/2011JA016477` doi: https://doi.org/10.1029/2011JA016477

Müller-Wodarg, I. C. F., Koskinen, T. T., Moore, L., Serigano, J., Yelle, R. V., Hörst, S., ... Mendillo, M. (2019). Atmospheric waves and their possible effect on the thermal structure of saturn's thermosphere. *Geophysical Research Letters*, *46*(5), 2372-2380. Retrieved from `https://agupubs.onlinelibrary.wiley.com/doi/abs/10.1029/2018GL081124` doi: https://doi.org/10.1029/2018GL081124

Oppenheim, M. M., Sugar, G., Slowey, N. O., Bass, E., Chau, J. L., & Close, S. (2009). Remote sensing lower thermosphere wind profiles using non-specular meteor echoes. *Geophysical Research Letters*, *36*(9). Retrieved from `https://agupubs.onlinelibrary.wiley.com/doi/abs/10.1029/2009GL037353` doi: https://doi.org/10.1029/2009GL037353

Oppenheim, M. M., vom Endt, A. F., & Dyrud, L. P. (2000). Electrodynamics of meteor trail evolution in the equatorial e-region ionosphere. *Geophysical Research Letters*, *27*(19), 3173-3176. Retrieved from `https://agupubs.onlinelibrary.wiley.com/doi/abs/10.1029/1999GL000013` doi: https://doi.org/10.1029/1999GL000013

Oyama, S., Shiokawa, K., Kurihara, J., Tsuda, T. T., Nozawa, S., Ogawa, Y., ... Watkins, B. J. (2010). Lower-thermospheric wind fluctuations measured with an fpi during pulsating aurora at tromsø, norway. *Annales Geophysicae*, *28*(10), 1847–1857. Retrieved from `https://angeo.copernicus.org/articles/28/1847/2010/` doi: 10.5194/angeo-28-1847-2010

Philbrick, C. P., Yang, F., Vargas, F. A., Swenson, G. R., & Liu, A. Z. (2021). A na density lidar method and measurements of turbulence to 105 km at the andes lidar observatory. *Journal of Atmospheric and Solar-Terrestrial Physics*, *219*, 105642. Retrieved from `https://www.sciencedirect.com/science/article/pii/S1364682621001000` doi: https://doi.org/10.1016/j.jastp.2021.105642

Prölss, G. W. (1980). Magnetic storm associated perturbations of the upper atmosphere: Recent results obtained by satellite-borne gas analyzers. *Reviews of Geophysics*, *18*(1), 183-202. Retrieved from `https://agupubs.onlinelibrary.wiley.com/doi/abs/10.1029/RG018i001p00183` doi: https://doi.org/10.1029/RG018i001p00183

Richmond, A. D. (1995). Ionosphere electrodynamics using apex coordinates. *Journal of Geomagnetism and Geoelectricity*, *47*, 191-212. doi: https://doi.org/10.5636/jgg.47.191

Ridley, A. J., Deng., Y., & Tóth, G. (2006). The global ionosphere thermosphere model. *Journal of Atmospheric and Solar-Terrestrial Physics*, *68*, 839–864.

Rishbeth, H., & Müller-Wodarg, I. C. F. (1999). Vertical circulation and thermospheric composition: a modeling study. *Ann. Geophysicae*, *17*(794–805).

Smith, R. W. (1998). Vertical winds: a tutorial. *J. Atmos. Sol. Terr. Phys.*, *60*, 1425–1434.

Spencer, N. W., Wharton, L. E., Carignan, G. R., & Maurer, J. C. (1982). Thermosphere zonal winds, vertical motions and temperature as measured from dynamics explorer. *Geophys. Res. Lett.*, *9*(9), 953–956.

Strugarek, D., Sośnica, K., & Jäggi, A. (2019). Characteristics of goce orbits based on satellite laser ranging. *Advances in Space Research*, *63*(1), 417-431. Retrieved from `https://www.sciencedirect.com/science/article/pii/S0273117718306616` doi: https://doi.org/10.1016/j.asr.2018.08.033

Touboul, P. (2003). Microscope instrument development, lessons for goce. *Space Science Reviews*, *108*, 393-408.

Visser, T., Doornbos, E., de Visser, C., Visser, P., & Fritsche, B. (2018). Torque model verification for the goce satellite. *Advances in Space Research*, *62*, 1114–1136.

Visser, T., March, G., Doornbos, E., de Visser, C., & Visser, P. (2019a). Horizontal and vertical thermospheric cross-wind from goce linear and angular accelerations. *Advances in Space Research*, *63*(10), 3139-3153. Retrieved from `https://www.sciencedirect.com/science/article/pii/S027311771930050X` doi: https://doi.org/10.1016/j.asr.2019.01.030

Visser, T., March, G., Doornbos, E. N., de Visser, C. C., & Visser, P. N. A. M. (2019b). Characterization of thermospheric vertical wind activity at 225-km to 295-km altitude using goce data and validation against explorer missions. *J. Geophys. Res.: Sp. Phys.*, *124*, 4852–4869.

Wang, W., Burns, A. G., Wiltberger, M., Solomon, S. C., & Killeen, T. L. (2008). Altitude variation of the horizontal thermospheric winds during geomagnetic storms. *Journal of Geophysical Research: Space Physics*, *113*.

Wang, W., Killeen, T. L., Burns, A. G., & Roble, R. G. (1999). A high resolution, three-dimensional, time dependent, nested grid model of the coupled thermosphere-ionosphere. , *61*, 385-397.

Weimer, D. R. (2005). Improved ionospheric electrodynamic models and application to calculating joule heating rates. *Journal of Geophysical Research: Space Physics*, *110*(A5). Retrieved from `https://agupubs.onlinelibrary.wiley.com/doi/abs/10.1029/2004JA010884` doi: https://doi.org/10.1029/2004JA010884

Weygand, J. M., Zesta, E., & Troshichev, O. (2014). Auroral electrojet indices in the northern and southern hemispheres: A statistical comparison. *Journal of Geophysical Research: Space Physics*, *119*(6), 4819-4840. Retrieved from `https://agupubs.onlinelibrary.wiley.com/doi/abs/10.1002/2013JA019377` doi: https://doi.org/10.1002/2013JA019377

Wiltberger, M., Wang, W., Burns, A. G., Burns, S. C., Solomon, S. C., Lyon, J. G., & Goodrich, C. C. (2004). Initial results from the coupled magnetosphere ionosphere thermosphere model: Magnetospheric amd ionospheric responses. *Journal of Atmospheric and Solar-Terrestrial Phyics*, *66*, 1411-1424.

Yao, X., Yu, T., Zhao, B., Yu, Y., Liu, L., Ning, B., & Wan, W. (2015). Climatological modeling of horizontal winds in the mesosphere and lower thermosphere over a mid-latitude station in china. *Advances in Space Research*, *56*(7), 1354-1365. Retrieved from `https://www.sciencedirect.com/science/article/pii/S0273117715004627` doi: https://doi.org/10.1016/j.asr.2015.06.026

Yiğit, E., & Ridley, A. J. (2011). Role of variability in determining the vertical wind speeds and structure. *J. Geophys. Res.*, *116*(A12305).

Yuan, W., Liu, X., Xu, J., Zhou, Q., Jiang, G., & Ma, R. (2013). Fpi observations of nighttime mesospheric and thermospheric winds in china and their comparisons with hwm07. *Annales Geophysicae*, *31*(8), 1365-1378. Retrieved from https://angeo.copernicus.org/articles/31/1365/2013/ doi: 10.5194/angeo-31-1365-2013

Zhao, S., Urbina, J., Dyrud, L., & Seal, R. (2011). Multilayer detection and classification of specular and nonspecular meteor trails. *Radio Science*, *46*(6). Retrieved from https://agupubs.onlinelibrary.wiley.com/doi/abs/10.1029/2010RS004548 doi: https://doi.org/10.1029/2010RS004548